Acta Crystallographica Section A
Foundations of Crystallography
ISSN 0108-7673

Received 24 May 2004
Accepted 2 February 2005

© 2005 International Union of Crystallography
Printed in Great Britain – all rights reserved

Quantitative structure retrieval at atomic resolution

N. L. O'Leary and L. J. Allen*

School of Physics, University of Melbourne, Victoria 3010, Australia. Correspondence e-mail: lja@physics.unimelb.edu.au

The ability to determine the structure of a sample at atomic resolution is crucial for the development of nanotechnology and materials science. Consequently, structure retrieval must become a quantitative rather than a qualitative exercise. A method to retrieve the projected potential of a crystalline sample by inversion from an exit-surface wavefunction in high-resolution electron microscopy is proposed. This method accounts for both multiple scattering and absorption.

1. Introduction

Recent developments in image interpretation methods in high-resolution electron microscopy allow the reconstruction of the exit-surface wavefunction (ESWF) of a crystalline sample at atomic resolution. The maximum-likelihood (MAL) method (Coene *et al.*, 1996) and the iterative wavefunction reconstruction (IWFR) method (Allen *et al.*, 2004*a*,*b*) reconstruct the ESWF from a series of images taken at different defocus values. These approaches also correct for coherent and incoherent aberrations in the microscope optics. However, at atomic resolution, images suffer the well known contrast problem and this is a barrier to quantitative structure retrieval (Hÿtch & Stobbs, 1994; Boothroyd *et al.*, 1995; Boothroyd, 1998). The contrast in experimental images is typically a factor (called the Stobbs factor) of three to five times less than that predicted by simulations (Howie, 2004).

There is much speculation as to the cause of the lack of contrast in atomic resolution images. Inelastic scattering, and in particular thermal diffuse scattering (TDS), has been suggested as the major reason for the reduction in contrast (Lehmann *et al.*, 2002). That being the case, the side band of an off-axis holography diffraction pattern should not be affected by the contrast problem as it contains only information from scattering events with an energy change of less than 10^{-15} eV (Van Dyck *et al.*, 2000), which excludes all inelastic scattering including TDS. The center band is affected by inelastic scattering, as is the case in high-resolution imaging. ESWFs can be obtained directly from the side and center bands (Orchowski *et al.*, 1995) and the contrast of the corresponding images can vary by as much as a factor of five (Lehmann *et al.*, 2002). We note, however, that other authors have not found such a large factor in similar circumstances (Boothroyd & Dunin-Borkowski, 2004). They suggest that inelastic scattering alone cannot explain the contrast problem in high-resolution imaging and that scattering from amorphous surface layers is also an important contribution.

Assuming the contrast problem can be circumvented, the important problem of obtaining the electron–object interaction can be tackled to obtain a quantitative measure of the structure of the object (Van Aert *et al.*, 2002), which is non-trivial when dynamical (multiple) scattering is significant. In particular, we wish to obtain the projected potential seen by the incoming electron beam. We propose an exact inversion scheme based on the solution of a set of non-linear equations to obtain the projected structure from the ESWF for a single orientation of the incident beam. The effect of inelastic scattering is accounted for and the inelastic scattering potential (mainly due to TDS) is also reconstructed. To illustrate the inversion method, we consider a model case of electrons incident on a thin silicon slab. The effect of a post-specimen aperture (which limits resolution in the image plane) and noise on the accuracy of the retrieved structure is investigated.

In the absence of strong dynamical scattering effects, approximate methods have been used to perform inversion from a single ESWF to obtain the projected potential. These methods include the weak-phase-object approximation and the pseudo-weak-phase-object approximation (Li & Tang, 1985). An iterative technique was developed to overcome the problems of image interpretation in the presence of dynamical scattering (Gribelyuk, 1991). This method was implemented to retrieve the elastic potential and is limited by sample thickness. A method based on the reversal of the multislice algorithm was proposed (Beeching & Spargo, 1993) and its limitations in terms of sample thickness investigated using a Bloch-wave analysis (Beeching *et al.*, 1994). A different approach considered an approximate channeling method (Op de Beeck & Van Dyck, 1996; Van Dyck & Geuens, 2002). This method works for large sample areas but is limited by thickness and is more successful for light atomic columns. Two inversion methods have been proposed that are based on changing an experimental parameter. The first is based on the principle that for small changes in the incident beam voltage the difference in diffraction intensities is proportional to the crystal potential (Rez, 1999). The second involved recovering the potential from the ESWFs obtained at two different thicknesses (Allen *et al.*, 2001). Both these methods are difficult to implement in practice.

Two methods based on optimization algorithms have been proposed recently. A scheme that uses simulated annealing to

compare an ESWF obtained from a trial projected potential with that of an experimental ESWF (Lentzen & Urban, 1996) was found to converge to the correct solution so long as the sample was not too thick. A later paper by the same authors uses a maximum-likelihood refinement (Lentzen & Urban, 2000). Two different approximations were used to obtain a starting guess for the minimization algorithm. The first was the weak-phase-object approximation. This failed to converge to the correct solution for test samples of thickness 100 Å. The second was an approximate channeling method. This improved the starting guess so that the routine converged for the 100 Å thick test samples. A disadvantage of both these methods is that optimization routines can fall into local minima and hence appear to converge, but to an incorrect solution. The solution of a set of non-linear equations, as is the case for the inversion method proposed here, has the advantage that it is always global in approach. Each step in non-linear equation solving algorithms refines the solution set in such a way that *all* equations simultaneously converge towards the solution, thus ameliorating the problem of local minima.

Several other authors have considered refinement techniques to determine structure factors. Many authors use convergent-beam electron diffraction (CBED) patterns, for example, Zuo & Spence (1991), Tsuda & Tanaka (1995) and Vincent & Exelby (1995). Standard electron diffraction patterns can be used in tandem with the well known multislice method and least-squares-fitting procedures to refine structural parameters (Sha *et al.*, 1993; Jansen *et al.*, 1998).

An approach where the inversion step can be reduced to the solution of a set of linear equations, thus ensuring a unique solution, has been proposed (Allen *et al.*, 1998). However, a through-tilt series of measurements is then needed to obtain the ESWFs for several orientations of the incident beam (Allen *et al.*, 1998; Spence, 1998), which is difficult to implement experimentally.

2. Inversion from a single ESWF

The scattering matrix relates the wave incident on the crystal to that at the exit surface. For a plane wave incident in an exact zone-axis orientation and normalized to unity, we can write (Allen *et al.*, 2000)

$$\begin{pmatrix} \vdots \\ v_{\mathbf{h}} \\ v_{\mathbf{g}} \\ v_{\mathbf{0}} \\ v_{-\mathbf{g}} \\ v_{-\mathbf{h}} \\ \vdots \end{pmatrix} = \begin{pmatrix} & \vdots & \vdots & \vdots & \\ \cdots & \mathcal{S}_{\mathbf{h},\mathbf{g}} & \mathcal{S}_{\mathbf{h},\mathbf{0}} & \mathcal{S}_{\mathbf{h},-\mathbf{g}} & \cdots \\ \cdots & \mathcal{S}_{\mathbf{g},\mathbf{g}} & \mathcal{S}_{\mathbf{g},\mathbf{0}} & \mathcal{S}_{\mathbf{g},-\mathbf{g}} & \cdots \\ \cdots & \mathcal{S}_{\mathbf{0},\mathbf{g}} & \mathcal{S}_{\mathbf{0},\mathbf{0}} & \mathcal{S}_{\mathbf{0},-\mathbf{g}} & \cdots \\ \cdots & \mathcal{S}_{-\mathbf{g},\mathbf{g}} & \mathcal{S}_{-\mathbf{g},\mathbf{0}} & \mathcal{S}_{-\mathbf{g},-\mathbf{g}} & \cdots \\ \cdots & \mathcal{S}_{-\mathbf{h},\mathbf{g}} & \mathcal{S}_{-\mathbf{h},\mathbf{0}} & \mathcal{S}_{-\mathbf{h},-\mathbf{g}} & \cdots \\ & \vdots & \vdots & \vdots & \end{pmatrix} \begin{pmatrix} \vdots \\ 0 \\ 0 \\ 1 \\ 0 \\ 0 \\ \vdots \end{pmatrix}, \quad (1)$$

where the indices on the elements of the scattering matrix $\mathcal{S}$ refer to reciprocal-lattice vectors in a plane perpendicular to the zone axis. It is clear that the Fourier coefficients $v_{\mathbf{g}}$ of the ESWF are directly related to the central column of $\mathcal{S}$ by $v_{\mathbf{g}} = \mathcal{S}_{\mathbf{g},\mathbf{0}}$. In an N-beam Bloch-wave formulation, $\mathcal{S}$ is an $N \times N$ complex matrix. Obtaining the ESWF for the exact zone-axis orientation provides us with the central column of $\mathcal{S}$. The remaining elements of $\mathcal{S}$ can be obtained *via* a series of tilts of the incident beam from the principal orientation by a reciprocal-lattice vector $\mathbf{g}$, *i.e.* by changing the position of the 1 in the column matrix on the right-hand side of equation (1).

The information about the structure of the sample is contained in the structure matrix $\mathcal{A}$, which we can write in the form (Allen *et al.*, 2000)

$$\mathcal{A} = \begin{pmatrix} & \vdots & \vdots & \vdots & \\ \cdots & W_{\mathbf{h}-\mathbf{g}} & W_{\mathbf{h}} & W_{\mathbf{h}+\mathbf{g}} & \cdots \\ \cdots & Q_{\mathbf{g}} & W_{\mathbf{g}} & W_{2\mathbf{g}} & \cdots \\ \cdots & W_{-\mathbf{g}} & Q_{\mathbf{0}} & W_{\mathbf{g}} & \cdots \\ \cdots & W_{-2\mathbf{g}} & W_{-\mathbf{g}} & Q_{-\mathbf{g}} & \cdots \\ \cdots & W_{-\mathbf{h}-\mathbf{g}} & W_{-\mathbf{h}} & W_{-\mathbf{h}+\mathbf{g}} & \cdots \\ & \vdots & \vdots & \vdots & \end{pmatrix}, \quad (2)$$

where $W_{\mathbf{g}}$ are the Fourier coefficients of the optical potential for the scattering of electrons by the crystal and for an exact zone-axis orientation

$$Q_{\mathbf{g}} = -\mathbf{g}^2 + iU_0'. \quad (3)$$

In this equation, U_0' is the mean absorption. The scattering matrix $\mathcal{S}$ can be obtained from the structure matrix $\mathcal{A}$ *via*

$$\mathcal{S}(\{W_{\mathbf{h}}\}) = \exp\left(\frac{i\pi t}{K}\mathcal{A}\right), \quad (4)$$

where t is the thickness of the specimen and K is the wavenumber of the incident electron corrected for refraction, *i.e.* $K^2 = k^2 + U_0$, with k the wavenumber in vacuum and U_0 the mean inner potential. The scattering matrix $\mathcal{S}$ is a function of the set of Fourier coefficients $\{W_{\mathbf{h}}\}$ in the structure matrix $\mathcal{A}$. Provided we have all columns in $\mathcal{S}$, equation (4) can be inverted to obtain the structure as follows:

$$\mathcal{A} = \frac{K}{i\pi t}\ln \mathcal{S}. \quad (5)$$

An ambiguity arises in this equation since the evaluation of the natural logarithm of the matrix $\mathcal{S}$ involves taking the natural logarithm of the complex eigenvalues of $\mathcal{S}$. This can be resolved by taking into account the known diagonals and fundamental symmetries in the $\mathcal{A}$ matrix, leading to a set of linear equations that can be solved using single-value decomposition (Allen *et al.*, 2000). This inversion easily provides a unique solution; however, there are problems associated with its practical implementation. Taking data at many accurately determined tilts of the incident beam is technically difficult, with a focal series required for ESWF reconstruction at each tilt. In addition, taking such large amounts of data may cause radiation damage to the sample. Retrieval using data at only one orientation of the incident beam would be advantageous. This means we need to proceed knowing only the central column of the scattering matrix $\mathcal{S}$. Assuming that we are working in an N-beam approximation, we have a set $\{\mathcal{S}_{\mathbf{g},\mathbf{0}}\}$ of N complex pieces of data at our disposal

to effect the inversion. Let us first consider this in the single scattering approximation, in which case

$$\mathcal{A} \approx \frac{K}{i\pi t}(\mathcal{S} - \mathcal{I}), \quad (6)$$

where $\mathcal{I}$ is the identity matrix. If the mean inner potential U_0 is not known, then we can make the approximation $K \approx k$ in the above equation. This is an excellent estimate since, for example, at an incident energy of 300 keV, $K = 50.797$ Å^{-1} and $k = 50.795$ Å^{-1}.

Using equations (1) and (2) in combination with equation (6), we can invert to obtain the Fourier coefficients of the potential in the central column of the $\mathcal{A}$ matrix *via*

$$W_{\mathbf{g}} \approx \frac{K}{i\pi t}\mathcal{S}_{\mathbf{g},\mathbf{0}}, \quad \mathbf{g} \neq \mathbf{0}, \quad (7)$$

assuming t has been independently determined, for example by analysis of CBED patterns (Kelly *et al.*, 1975; Allen, 1981). In practice, $\mathcal{S}_{\mathbf{g},\mathbf{0}}$ cannot be directly obtained from $v_{\mathbf{g}}$ since the intensity of the incident beam is not accurately known [we have assumed it is normalized to one in equation (1)]. Furthermore, the ESWF can only be determined up to an arbitrary overall phase constant ϕ. These problems affect the recovered ESWF regardless of the method used to obtain it. To see how these two problems may be circumvented, we write the Fourier coefficients of the ESWF obtained in practice, in terms of those in equation (1), in the form

$$v'_{\mathbf{g}} = \alpha v_{\mathbf{g}} \exp(i\phi), \quad (8)$$

where α is a normalization constant. We then obtain $\mathcal{S}_{\mathbf{g},\mathbf{0}}$, required for the inversion in equation (7), from

$$\mathcal{S}_{\mathbf{g},\mathbf{0}} = \mathcal{S}_{\mathbf{0},\mathbf{0}}\frac{v_{\mathbf{g}}}{v_{\mathbf{0}}} = \mathcal{S}_{\mathbf{0},\mathbf{0}}\frac{v'_{\mathbf{g}}}{v'_{\mathbf{0}}} \approx \left(1 - \frac{\pi t}{K}U'_{\mathbf{0}}\right)\frac{v'_{\mathbf{g}}}{v'_{\mathbf{0}}}. \quad (9)$$

Assuming that t is known and that we have an estimate for the mean absorption $U'_{\mathbf{0}}$, we can calculate $\mathcal{S}_{\mathbf{g},\mathbf{0}}$ in the single scattering approximation, correct in both magnitude and phase.

Diagonal terms of the form $-\mathbf{g}^2 + iU'_0$

	0	$1\bar{1}\bar{1}$	0	$1\bar{1}\bar{3}$	0	$00\bar{4}$	$\bar{1}1\bar{3}$	0	0	0	$\bar{1}1\bar{1}$	0
0		0	$1\bar{1}3$	004	0	$\bar{1}13$	0	0	0	$\bar{2}20$	0	$\bar{1}1\bar{1}$
$\bar{1}11$	0		$1\bar{1}\bar{3}$	0	$00\bar{4}$	$\bar{1}1\bar{3}$	0	0	0	0	$\bar{2}20$	0
0	$\bar{1}1\bar{3}$	$\bar{1}13$		$\bar{1}11$	$\bar{1}1\bar{1}$	$\bar{2}20$	0	0	0	0	0	0
$\bar{1}1\bar{3}$	$00\bar{4}$	0	$1\bar{1}\bar{1}$		0	$\bar{1}1\bar{1}$	$\bar{2}20$	0	0	0	0	0
0	0	004	$1\bar{1}1$	0		$\bar{1}11$	0	$\bar{2}20$	0	0	0	$\bar{1}1\bar{3}$
004	$1\bar{1}\bar{3}$	$1\bar{1}3$	$2\bar{2}0$	$1\bar{1}1$	$1\bar{1}\bar{1}$		$\bar{1}11$	$\bar{1}1\bar{1}$	$\bar{2}20$	$\bar{1}1\bar{3}$	$\bar{1}13$	$00\bar{4}$
$1\bar{1}3$	0	0	0	$2\bar{2}0$	0	$1\bar{1}\bar{1}$		0	$\bar{1}1\bar{1}$	$00\bar{4}$	0	0
0	0	0	0	0	$2\bar{2}0$	$1\bar{1}1$	0		$\bar{1}11$	0	004	$1\bar{1}\bar{3}$
0	0	0	0	0	0	$2\bar{2}0$	$1\bar{1}1$	$1\bar{1}\bar{1}$		$1\bar{1}\bar{3}$	$1\bar{1}3$	0
0	$2\bar{2}0$	0	0	0	0	$1\bar{1}3$	004	0	$\bar{1}13$		0	$1\bar{1}\bar{1}$
$1\bar{1}1$	0	$2\bar{2}0$	0	0	0	$1\bar{1}\bar{3}$	0	$00\bar{4}$	$\bar{1}1\bar{3}$	0		0
0	$1\bar{1}1$	0	0	0	$1\bar{1}3$	004	0	$\bar{1}1\bar{3}$	0	$\bar{1}11$	0	

Figure 1
The structure of the $\mathcal{A}$ matrix for silicon along the [110] zone axis in an $N = 13$ beam approximation. Only elements that occur in the central column are retained elsewhere and higher-order coefficients are assumed to be zero (those indicated by a single 0).

Single scattering usually applies for small thicknesses, so that the term in brackets is approximately unity and explicit knowledge of $U'_{\mathbf{0}}$ is not essential.

Let us now generalize this to the case of multiple scattering. As before, we start with an ESWF which in principle has been obtained from experiment. From the Fourier coefficients of the ESWF, we construct the $N - 1$ complex quantities $\mathcal{S}_{\mathbf{g},\mathbf{0}}/\mathcal{S}_{\mathbf{0},\mathbf{0}}$. The central column of the $\mathcal{A}$ matrix also contains $N - 1$ complex Fourier coefficients. Fourier coefficients not in the central column of $\mathcal{A}$ are higher-order Fourier coefficients of the potential and are assumed to be small enough to be neglected. We illustrate this procedure in Fig. 1, which shows the indexing of the Fourier coefficients for the [110] zone axis in silicon in an $N = 13$ beam approximation. There are $N - 1 = 12$ complex Fourier coefficients in the central column of the structure matrix that are retained elsewhere. Elements which, by indexing, are found to be higher-order Fourier coefficients are indicated by a single 0 in Fig. 1.

We can write down the following $N - 1$ non-linear equations in terms of the set of $N - 1$ unknown complex Fourier coefficients $\{W_{\mathbf{h}}\}$:

$$F_{\mathbf{g}}(\{W_{\mathbf{h}}\}) = \left[\frac{\mathcal{S}_{\mathbf{g},\mathbf{0}}}{\mathcal{S}_{\mathbf{0},\mathbf{0}}}\right]^{\exp} - \left[\frac{\mathcal{S}_{\mathbf{g},\mathbf{0}}(\{W_{\mathbf{h}}\})}{\mathcal{S}_{\mathbf{0},\mathbf{0}}(\{W_{\mathbf{h}}\})}\right]^{\text{theory}} = 0, \quad (10)$$

where the ratio $[\mathcal{S}_{\mathbf{g},\mathbf{0}}(\{W_{\mathbf{h}}\})/\mathcal{S}_{\mathbf{0},\mathbf{0}}(\{W_{\mathbf{h}}\})]^{\text{theory}}$ can be extracted from the scattering matrix $\mathcal{S}(\{W_{\mathbf{h}}\})$ that is evaluated using equation (4) (where, as discussed previously, we may need to use the approximation $K \approx k$). These non-linear equations can be solved using standard routines, for example those based on Broyden's method. This method is a multidimensional generalization of the one-dimensional secant method (Press *et al.*, 1986; Kelly, 1995). We wish to emphasize that this is not an optimization procedure. One might be tempted to define a master function $F(\{W_{\mathbf{h}}\})$, which is the sum of the squares of the individual functions $F_{\mathbf{g}}(\{W_{\mathbf{h}}\})$, is positive definite and has a global minimum at the roots of the non-linear equations. However, such a procedure can come to rest on local or global minima without discretion. The reason for this is that a minimization routine can 'go downhill' by a dominant decrease in one term in the master function. Each iteration in a multidimensional root-finding method requires that all $N - 1$ equations simultaneously head towards a better solution. Hence the formulation of this problem in terms of $N - 1$ non-linear equations in terms of $N - 1$ unknown Fourier coefficients of the optical potential is significant. However, despite the robustness of Broyden's method, it does not necessarily guarantee a solution. As a starting estimate for the solution to the set of non-linear equations, we can use a single scattering approximation.

3. Model inversions

3.1. No aperture and no noise

As has been done by the authors whose methods are discussed in the *Introduction* (Gribelyuk, 1991; Beeching & Spargo, 1993; Lentzen & Urban, 1996; Op de Beeck & Van

Dyck, 1996; Rez, 1999; Lentzen & Urban, 2000; Allen *et al.*, 2001), the inversion method proposed here will be illustrated using simulated data. The method was tested for a variety of simulated specimens. The two cases shown here are silicon and silicon nitride, the latter having an hexagonal symmetry. The effect of a post-specimen aperture and noise in the ESWF on the retrieved potential will also be considered later.

We have simulated a focal series of images using the Bloch-wave method for 300 keV electrons incident on a 120 Å thick slab of silicon along the [110] zone-axis direction. With $N = 157$, there are 156 complex Fourier coefficients of the optical potential in the central column of the $\mathcal{A}$ matrix. Inelastic scattering is assumed to arise solely from TDS and was calculated using the Einstein model (Allen & Rossouw, 1989; Bird & King, 1990). The projected potential for elastic scattering [Fourier coefficients $U_{\mathbf{g}} = (W_{\mathbf{g}} + W^{*}_{-\mathbf{g}})/2$] is shown in Fig. 2(*a*). That for inelastic scattering [Fourier coefficients $U_{\mathbf{g}'} = (W_{\mathbf{g}} - W^{*}_{-\mathbf{g}})/2i$] is shown in Fig. 2(*b*). A focal series of images for a crystal of thickness $t = 120$ Å is shown in Fig. 2(*c*). The defocus value of each image is given in the figure, the negative values denoting underfocus.

The IWFR (Allen *et al.*, 2004*a*) method was applied to this focal series to produce the ESWF shown in Fig. 2(*d*), displayed in the form of an image and phase map. The phase map shown has values approximately 0.2 rad greater than those of the correct ESWF, *i.e.* $\phi \approx 0.2$ rad in equation (8). At this stage in our discussion, let us assume that we know the flux of the incident beam and that $|\mathcal{S}_{\mathbf{0},\mathbf{0}}|$ (≈ 0.5) has been determined from the diffraction pattern and, initially, that $\mathcal{S}_{\mathbf{0},\mathbf{0}}$ is real. (We will not make the assumption that $|\mathcal{S}_{\mathbf{0},\mathbf{0}}|$ is known in §§3.2 and 3.3, where we consider more realistic experimental situations.) We then estimate $[\mathcal{S}_{\mathbf{g},\mathbf{0}}(\{W_{\mathbf{h}}\})/\mathcal{S}_{\mathbf{0},\mathbf{0}}(\{W_{\mathbf{h}}\})]^{\rm theory}$ using the single scattering approximation equation (7). The elastic and inelastic scattering potentials corresponding to this starting point are shown in Figs. 2(*e*) and 2(*f*), respectively. We have assumed that $W_{\mathbf{0}} = 0$, which we expect to essentially shift the elastic and inelastic potentials shown by U_0 and U_0', respectively, but notwithstanding this the agreement with the input potentials is not good.

By solving the non-linear equations, equation (10), we recover not only the input elastic potential, as shown in Fig. 2(*g*), but also the inelastic scattering potential, as shown in Fig. 2(*h*). These results are in excellent agreement with the starting model potentials except that, as revealed by closer inspection, the elastic potential is shifted downwards by ~ 14 eV and the inelastic potential by ~ 0.1 eV, U_0 and U_0' having once again been assumed to be zero, since they are not determined in the inversion. In principle, both U_0 and U_0' could be determined independently. The single scattering approximation provides a satisfactory starting guess for the non-linear equation solver we used (based on Broyden's method) out to around 150 Å. Thereafter, a better guess, such as the channeling approach (Lentzen & Urban, 2000), is needed.

As the thickness of the sample must be determined independently, it is important to demonstrate the robustness of the method if the thickness is not known accurately. Fig. 3(*a*) shows that there is little change in the elastic potential

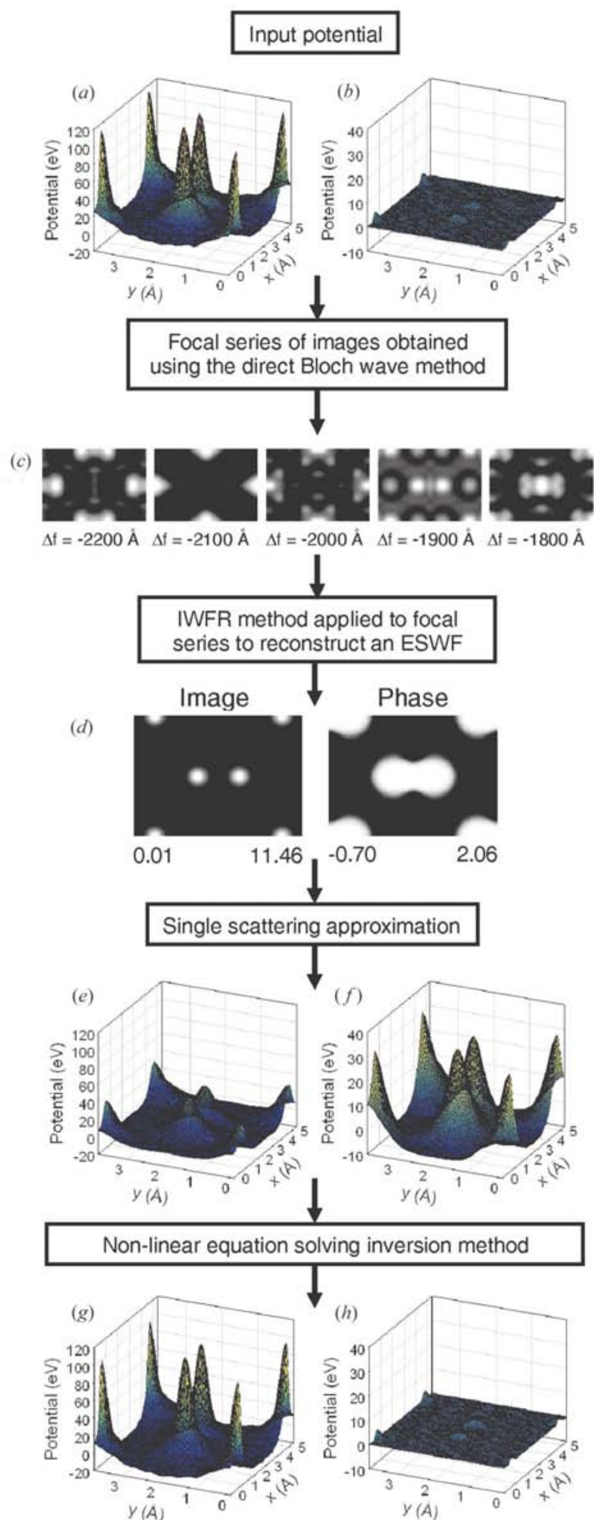

Figure 2
The input (*a*) elastic and (*b*) inelastic components of the projected potential for silicon with 300 keV electrons incident along the [110] zone-axis direction for a thickness of 120 Å. (*c*) A focal series of images obtained using the direct Bloch-wave method. The defocus values are shown under the images (the negative values indicate underfocus). (*d*) An ESWF obtained from the IWFR method. Results are shown for the reconstruction of the (*e*) elastic and (*f*) inelastic components of the projected potential using the single scattering approximation and the (*g*) elastic and (*h*) inelastic components of the projected potential using the non-linear equation solving inversion method.

obtained from the ESWF if the thickness is varied by as much as 20 Å either side of the nominal value of 120 Å. However, Fig. 3(*b*) shows that the inelastic potential cannot be retrieved with accuracy unless the thickness is known precisely.

The second example shown is that of β-Si_3N_4. The focal series for this example was simulated in the same manner as the first with 300 keV electrons incident on a 100 Å thick slab along the [0001] zone-axis direction. With $N = 97$, there are 96 complex Fourier coefficients of the optical potential in the central column of the $\mathcal{A}$ matrix in this case.

The components of the projected potential for elastic scattering and inelastic scattering are shown in Figs. 4(*a*) and 4(*b*), respectively. The five images in the focal series are shown in Fig. 4(*c*). As previously described, the IWFR method was applied to the focal series to produce the ESWF shown in Fig. 4(*d*), displayed as an image and phase map. A starting guess for the potential was generated using the single scattering approximation and the elastic and inelastic scattering potentials are shown in Figs. 4(*e*) and 4(*f*). Once again, the non-linear equations are solved to obtain the elastic and inelastic potentials shown in Figs. 4(*g*) and 4(*h*), which show excellent agreement with the input potentials shown in the same figure. Closer inspection reveals that there is a shift of ~ 0.1 eV in the inelastic potential, for the same reason there was a similar shift in the case of Si.

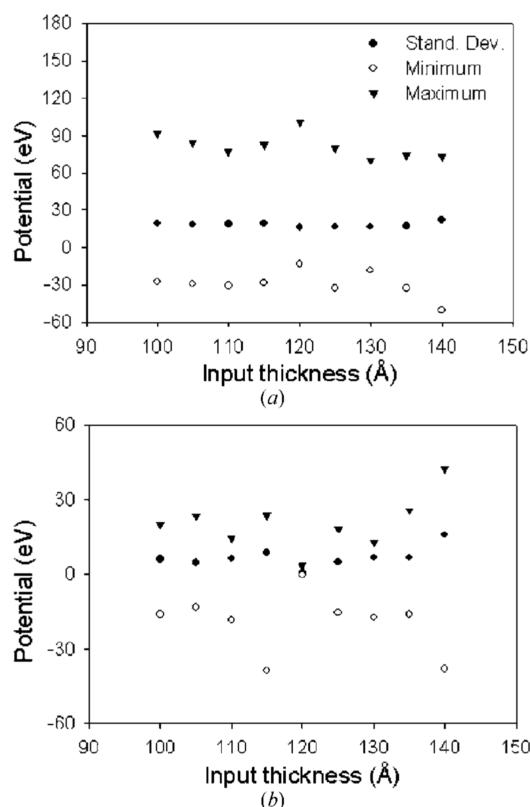

Figure 3
A measure of the standard deviation, minimum and maximum of the projected potential obtained from the ESWF using the non-linear equation solving inversion method for an Si sample of nominal thickness 120 Å if the thickness is not precisely known and varied within the range shown. Results are shown for the (*a*) elastic and (*b*) inelastic components of the projected potential.

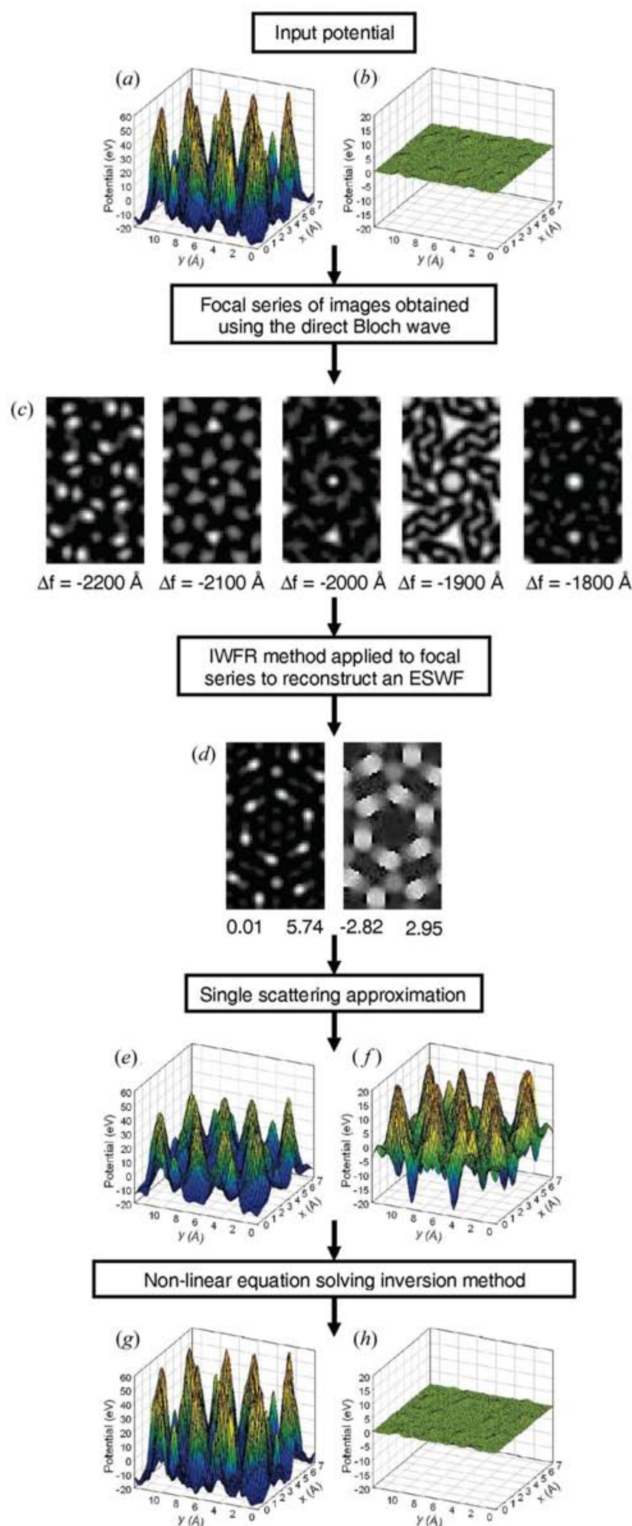

Figure 4
The input (*a*) elastic and (*b*) inelastic components of the projected potential for β-Si_3N_4 with 300 keV electrons incident along the [0001] zone-axis direction for a thickness of 100 Å. (*c*) A focal series of images obtained using the direct Bloch-wave method. The defocus values are shown under the images (the negative values indicate underfocus). (*d*) An ESWF obtained from the IWFR method. Results are shown for the reconstruction of the (*e*) elastic and (*f*) inelastic components of the projected potential using the single scattering approximation and the (*g*) elastic and (*h*) inelastic components of the projected potential using the non-linear equation solving inversion method.

3.2. Aperture and no noise

Let us now assume that the ESWF for Si in § 3.1 is obtained from a focal series of images that are modified by an objective aperture. The simulated focal series of images is shown in Fig. 5(*a*). The modified ESWF shown in Fig. 5(*b*) is obtained by applying the IWFR method (Allen *et al.*, 2004*a*) discussed earlier.

We no longer assume that $|\mathcal{S}_{\mathbf{0},\mathbf{0}}|$ is known. The $\mathcal{S}_{\mathbf{g},\mathbf{0}}$ in the single scattering inversion equation (7) are calculated from equation (9) taking $\mathcal{S}_{\mathbf{0},\mathbf{0}} = 1$. The resultant elastic projected potential is shown in Fig. 5(*c*) and the inelastic potential in Fig. 5(*d*). The non-linear equation solving inversion method proceeds as before by finding the roots of the set of equations defined by equation (10). The results are shown in Fig. 5(*e*) for the elastic potential and Fig. 5(*f*) for the inelastic potential. Both components of the potential are less resolved than the result obtained prior to the application of the aperture. The elastic component is damped down but the inelastic component has increased in size, confirming that the aperture is effectively an absorption mechanism.

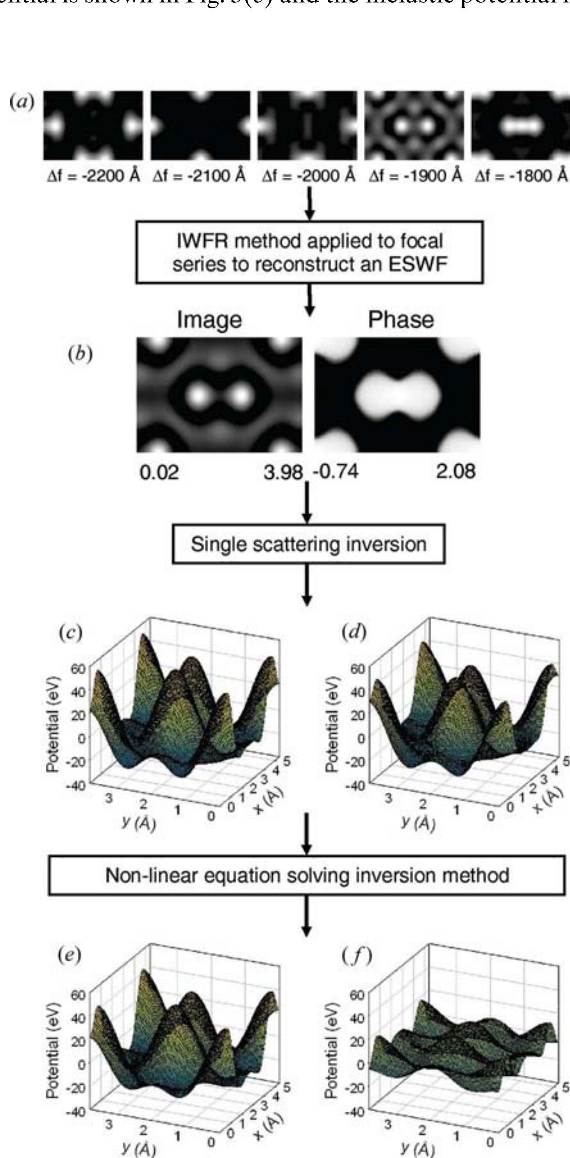

Figure 5
(*a*) Input focal series of images for Si as described in the text (a 14.6 mrad aperture has been applied). The defocus values are shown under the images (the negative values indicate underfocus). (*b*) The ESWF obtained by the IWFR method when applied to the focal series. The intensity range and phase range (in radians) are shown. Results are shown for the reconstruction of the (*c*) elastic and (*d*) inelastic components of the projected potential using the single scattering approximation and the (*e*) elastic and (*f*) inelastic components of the projected potential using the non-linear equation solving inversion method.

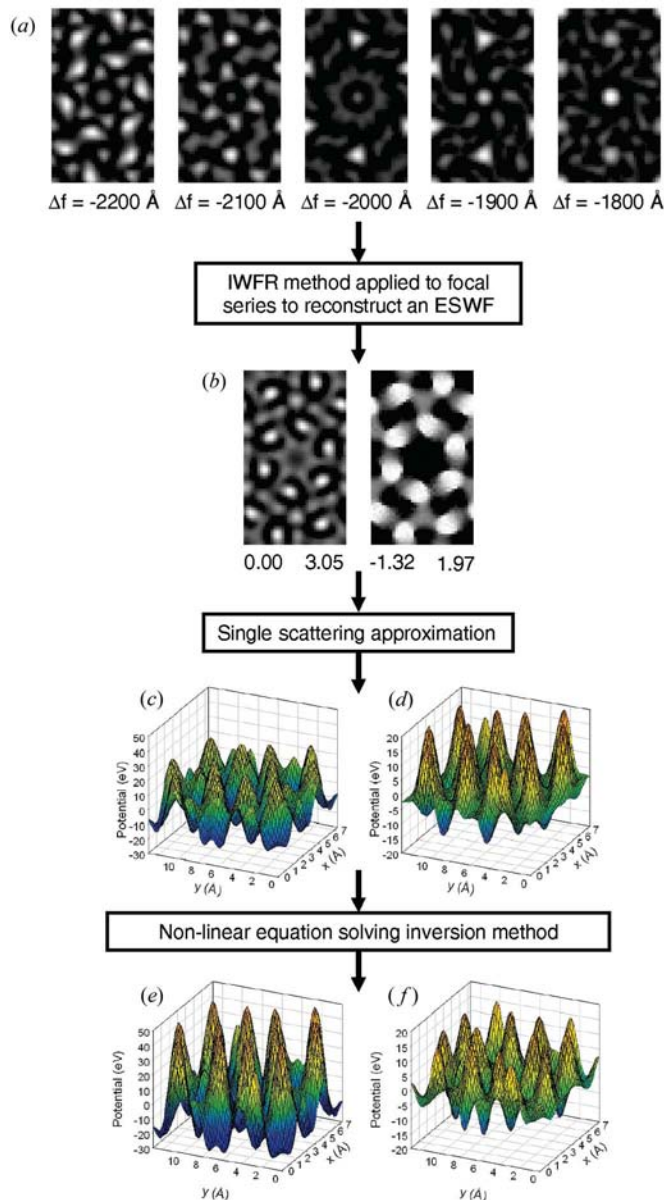

Figure 6
(*a*) Input focal series of images for β-Si_3N_4 (a 12.8 mrad aperture has been applied). The defocus values are shown under the images (the negative values indicate underfocus). (*b*) The ESWF obtained by the IWFR method when applied to the focal series. The intensity range and phase range (in radians) are shown. Results are shown for the reconstruction of the (*c*) elastic and (*d*) inelastic components of the projected potential using the single scattering approximation and the (*e*) elastic and (*f*) inelastic components of the projected potential using the non-linear equation solving inversion method.

The effect of an aperture for the β-Si_3N_4 case is shown in Fig. 6. The focal series of images in Fig. 6(*a*) has been modified by an aperture of size 12.8 mrad and the ESWF retrieved using the IWFR method is shown in Fig. 6(*b*). Starting from the single scattering approximation shown in Figs. 6(*c*) and 6(*d*), we obtain the elastic potential shown in Fig. 6(*e*), which is damped down by the aperture (but less than for the Si example), and the inelastic potential shown in Fig. 6(*f*), which once again illustrates the absorptive nature of the aperture.

3.3. Aperture with noise

To test the effects of noise on the outcome of this method, we used the focal series of five Si images in §3.2, shown in Fig. 5(*a*). Noise was added to the focal series by assigning a number of counts to each pixel assuming that the maximum intensity in the images corresponded to 400 counts. This corresponds to noise at the level of 5% for maximum intensity (with larger errors, of course, for all other pixels). The statistical errors at each pixel were assigned using a random deviate drawn from a Poisson distribution with mean corresponding to the noise-free number of counts for a given pixel (Press *et al.*, 1986). For example, the $\Delta f = -1900$ Å image in the focal series is shown in Fig. 7(*a*) prior to the addition of noise and Fig. 7(*b*) after the addition of noise. The ESWF was then retrieved using the IWFR method and the image is shown in Fig. 7(*c*) and the phase map in Fig. 7(*d*).

After applying the non-linear equation solving inversion method, we obtain a result that does not vary significantly from the result obtained prior to the inclusion of noise. In fact, there is no discernible difference from the results shown in Figs. 5(*e*) and 5(*f*) on the scale of these figures.

We also tested the effects of noise on the β-Si_3N_4 case study by applying noise, in the same way as for the Si case, to the focal series of images shown in Fig. 6(*a*). For comparison, the $\Delta f = -1900$ Å image in the focal series is shown in Fig. 8(*a*) prior to the addition of noise and Fig. 8(*b*) after the addition of noise. The ESWF was then retrieved using the IWFR method, as before, and the image is shown in Fig. 8(*c*) and the phase map in Fig. 8(*d*). As in the case of Si, there was no discernible difference from the results shown in Figs. 6(*e*) and 6(*f*) on the scale of these figures.

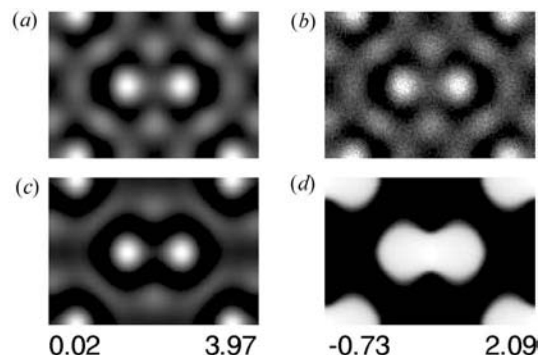

Figure 7
(*a*) The image in Fig. 5(*a*) with defocus $\Delta f = -1900$ Å and (*b*) with noise added as described in the text. (*c*) Image and (*d*) phase at the exit surface obtained from the noisy images.

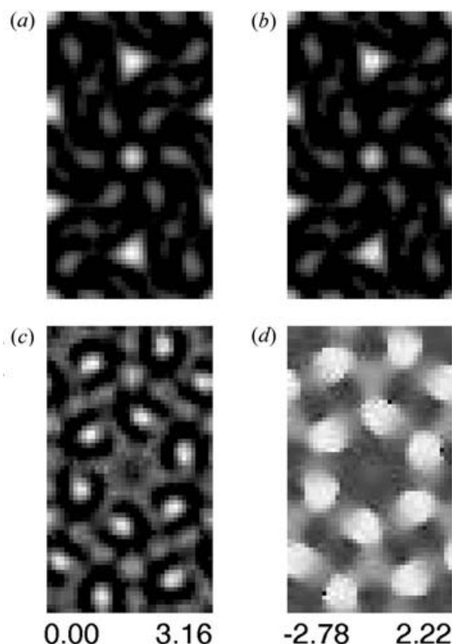

Figure 8
(*a*) The image in Fig. 6(*a*) with defocus $\Delta f = -1900$ Å and (*b*) with noise added as described in the text. (*c*) Image and (*d*) phase at the exit surface obtained from the noisy images.

4. Conclusions

We have discussed the importance of quantitative structure retrieval, especially in cases where dynamical scattering is significant. The lack of contrast in atomic resolution experimental images when compared to the best theoretical simulations remains a major barrier to quantitative structure interpretation, although off-axis electron holography promises to ameliorate this problem (Howie, 2004). Provided that this barrier can be overcome, the inversion method described in this paper is a readily implementable procedure for retrieving both the elastic and inelastic projected potentials of a crystalline sample from an ESWF obtained under dynamical conditions for a single orientation of the incident beam.

The authors would like to thank S. D. Findlay, W. McBride and M. P. Oxley for helpful discussions. L. J. Allen acknowledges the financial support of the Australian Research Council.

References

Allen, L. J., Faulkner, H. M. L. & Leeb, H. (2000). *Acta Cryst.* A**56**, 119–126.
Allen, L. J., Josefsson, T. W. & Leeb, H. (1998). *Acta Cryst.* A**54**, 388–398.
Allen, L. J., Koch, C., Oxley, M. P. & Spence, J. C. H. (2001). *Acta Cryst.* A**57**, 473–474.
Allen, L. J., McBride, W., O'Leary, N. L. & Oxley, M. P. (2004*a*). *Ultramicroscopy*, **100**, 91–104.

Allen, L. J., McBride, W., O'Leary, N. L. & Oxley, M. P. (2004*b*). *J. Microsc.* **216**, 70–75.

Allen, L. J. & Rossouw, C. J. (1989). *Phys. Rev. B*, **39**, 8313–8321.

Allen, S. M. (1981). *Philos. Mag.* A**43**, 325–335.

Beeching, M. J. & Spargo, A. E. C. (1993). *Ultramicroscopy*, **52**, 243–247.

Beeching, M. J., Spargo, A. E. C. & Allen, L. J. (1994). *Ultramicroscopy*, **55**, 329–333.

Bird, D. M. & King, Q. A. (1990). *Acta Cryst.* A**46**, 202–208.

Boothroyd, C. B. (1998). *J. Microsc.* **190**, 99–108.

Boothroyd, C. B. & Dunin-Borkowski, R. E. (2004). *Ultramicroscopy*, **98**, 115–133.

Boothroyd, C. B., Dunin-Borkowski, R. E., Stobbs, W. M. & Humphreys, C. J. (1995). *Mater. Res. Soc. Symp. Proc.* **354**, 495–500.

Coene, W. M. J., Thust, A., Op de Beeck, M. & Van Dyck, D. (1996). *Ultramicroscopy*, **64**, 109–135.

Gribelyuk, M. A. (1991). *Acta Cryst.* A**47**, 715–723.

Howie, A. (2004). *Ultramicroscopy*, **98**, 73–79.

Hÿtch, M. J. & Stobbs, W. M. (1994). *Ultramicroscopy*, **53**, 191–203.

Jansen, J., Tang, D., Zandbergen, H. W. & Schenk, H. (1998). *Acta Cryst.* A**54**, 91–101.

Kelly, C. T. (1995). *Iterative Methods for Linear and Nonlinear Equations*, Vol. 16 of *Frontiers in Applied Mathematics.* Philadelphia: SIAM.

Kelly, P. M., Jostons, A., Blake, R. G. & Napier, J. G. (1975). *Phys. Status Solidi A*, **31**, 771–780.

Lehmann, M., Geiger, D., Buscher, I., Zandbergen, H. W., Van Dyck, D., Lichte, H. & Spence, J. C. H. (2002). *Proceedings of the 15th International Congress on Electron Microscopy*, edited by J. Engelbrecht, T. Sewell, M. Witcomb, R. Cross & P. Richards, Vol. 3, pp. 279–280. Onderstepoort: Microscopy Society of Southern Africa.

Lentzen, M. & Urban, K. (1996). *Ultramicroscopy*, **62**, 89–102.

Lentzen, M. & Urban, K. (2000). *Acta Cryst.* A**56**, 235–247.

Li, F. H. & Tang, D. (1985). *Acta Cryst.* A**41**, 376–382.

Op de Beeck, M. & Van Dyck, D. (1996). *Ultramicroscopy*, **64**, 153–165.

Orchowski, A., Rau, W. D. & Lichte, H. (1995). *Phys. Rev. Lett.* **74**, 399–402.

Press, W. H., Teukolsky, S. A., Vetterling, W. T. & Flannery, B. P. (1986). *Numerical Recipes in Fortran: the Art of Scientific Computing*, 2nd ed. Cambridge University Press.

Rez, P. (1999). *Acta Cryst.* A**55**, 160–167.

Sha, B. D., Fan, H. F. & Li, F. H. (1993). *Acta Cryst.* A**49**, 877–880.

Spence, J. C. H. (1998). *Acta Cryst.* A**54**, 7–18.

Tsuda, K. & Tanaka, M. (1995). *Acta Cryst.* A**51**, 7–19.

Van Aert, S., den Dekker, A. J., van den Bos, A. & Van Dyck, D. (2002). *IEEE Trans. Instrum. Meas.* **51**, 611–615.

Van Dyck, D. & Geuens, P. (2002). *Proceedings of the 15th International Congress on Electron Microscopy*, edited by J. Engelbrecht, T. Sewell, M. Witcomb, R. Cross & P. Richards, Vol. 3, pp. 177–178. Onderstepoort: Microscopy Society of Southern Africa.

Van Dyck, D., Lichte, H. & Spence, J. C. H. (2000). *Ultramicroscopy*, **81**, 187–194.

Vincent, R. & Exelby, D. R. (1995). *Acta Cryst.* A**51**, 801–809.

Zuo, J. M. & Spence, J. C. H. (1991). *Ultramicroscopy*, **35**, 185–196.